Monthly Notices of the ROYAL ASTRONOMICAL SOCIETY

Mon. Not. R. Astron. Soc. **408,** 1916–1927 (2010) doi:10.1111/j.1365-2966.2010.17258.x

Full lensing analysis of Abell 1703: comparison of independent lens-modelling techniques

Adi Zitrin,[1★] Tom Broadhurst,[1,2,3] Keiichi Umetsu,[4] Yoel Rephaeli,[1] Elinor Medezinski,[1] Larry Bradley,[5] Yolanda Jiménez-Teja,[6] Narciso Benítez,[6] Holland Ford,[7] Jori Liesenborgs,[8] Sven De Rijcke,[9] Herwig Dejonghe[9] and Philippe Bekaert[8]

[1] *School of Physics and Astronomy, Raymond and Beverly Sackler Faculty of Exact Sciences, Tel Aviv University, Tel Aviv 69978, Israel*
[2] *Department of Theoretical Physics, University of Basque Country UPV/EHU, Leioa, Spain*
[3] *IKERBASQUE, Basque Foundation for Science, 48011 Bilbao, Spain*
[4] *Institute of Astronomy and Astrophysics, Academia Sinica, PO Box 23-141, Taipei 10617, Taiwan*
[5] *Space Telescope Science Institute, 3700 San Martin Drive, Baltimore, MD 21218, USA*
[6] *Instituto de Astrofísica de Andalucía (CSIC), C/Camino Bajo de Huétor 24, Granada 18008, Spain*
[7] *Department of Physics and Astronomy, Johns Hopkins University, 3400 North Charles Street, Baltimore, MD 21218, USA*
[8] *Expertisecentrum voor Digitale Media, Universiteit Hasselt, Wetenschapspark 2, B-3590 Diepenbeek, Belgium*
[9] *Sterrenkundig Observatorium, Universiteit Gent, Krijgslaan 281, S9, B-9000 Gent, Belgium*

Accepted 2010 June 25. Received 2010 June 23; in original form 2010 April 26

ABSTRACT

The inner mass profile of the relaxed cluster Abell 1703 is analysed by two very different strong-lensing techniques applied to the deep Advanced Camera for Surveys and the Wide Field Channel 3 imaging. Our parametric method has the accuracy required to reproduce many sets of multiple images, based on the assumption that mass approximately traces light. We test this assumption with a fully non-parametric, adaptive grid method, with no knowledge of the galaxy distribution. Differences between the methods are seen on fine scales due to member galaxies which must be included in models designed to search for lensed images, but on the larger scale the general distribution of dark matter is in good agreement, with very similar radial mass profiles. We add undiluted weak-lensing measurements from deep multicolour *Subaru* imaging to obtain a fully model-independent mass profile out to the virial radius and beyond. Consistency is found in the region of overlap between the weak and strong lensing, and the full mass profile is well described by a Navarro, Frenk & White (NFW) model of a concentration parameter, $c_{\rm vir} \simeq 7.15 \pm 0.5$ (and $M_{\rm vir} \simeq 1.22 \pm 0.15 \times 10^{15}\,{\rm M}_{\odot}\,h^{-1}$). Abell 1703 lies above the standard *c–M* relation predicted for the standard Λ cold dark matter model, similar to other massive relaxed clusters with accurately determined lensing-based profiles.

Key words: gravitational lensing: strong – galaxies: clusters: general – galaxies: clusters: individual: Abell 1703 – galaxies: elliptical and lenticular, cD – galaxies: formation – dark matter.

1 INTRODUCTION

Simulated cold dark matter (CDM) dominated haloes consistently predict mass profiles that steepen with radius, providing a distinctive, fundamental prediction for this form of dark matter (DM; Navarro, Frenk & White 1996, hereafter NFW). Furthermore, the degree of mass concentration should decline with increasing cluster mass because in the hierarchical model massive clusters collapse later, when the cosmological background density is lower. These predictions are now being subject to stringent lensing-based analyses, using multiply-lensed images and with weak-lensing (WL) information. To date only a few clusters have been reliably analysed by combining both weak and strong lensing for a full determination of the mass profile and a definitive comparison with predictions (e.g. Gavazzi et al. 2003; Broadhurst et al. 2005a, 2008; Newman et al. 2009; Okabe et al. 2010; Umetsu et al. 2010 and references therein). The upcoming multicycle *Hubble Space Telescope* (*HST*) programme of cluster imaging (the CLASH programme[1]) will provide a much more definitive derivation of mass

---

★E-mail: adiz@wise.tau.ac.il

[1] PI: Postman; http://www.stsci.edu/~postman/CLASH/

profiles for a statistical sample of relaxed, X-ray-selected clusters, combining high-resolution space imaging with deep, wide-field ground-based data.

Strong gravitational lensing (SL) is of great significance as a cosmological probe, providing model-free masses of galaxies and clusters interior to the Einstein radius and useful constraints on their inner mass profiles. The mass density in the central regions of distant clusters typically exceeds the critical value required for lensing, generating multiple images of background objects (e.g. Horesh et al. 2010; Kausch et al. 2010). Recent analyses have shown that many sets of multiply-lensed images can be uncovered with high-quality space imaging and thanks to improved modelling techniques. Reliable mass maps are claimed for several well-studied clusters with deep space imaging (e.g. Abell 370, Kneib et al. 1993; Richard et al. 2010; Abell 611 Newman et al. 2009; Abell 901, Deb et al. 2010; Abell 1689, Broadhurst et al. 2005b; Coe et al. 2010; Cl0024+1654, Liesenborgs et al. 2008; Zitrin et al. 2009b; MS 2137.3−2353, Gavazzi et al. 2003; Merten et al. 2009; RXJ1347, Bradač et al. 2008; Halkola et al. 2008; SDSS J1004+4112, Sharon et al. 2005; 'The bullet cluster', Bradač et al. 2006).

It is important to realize that most published mass maps usually adopt an initial model gradient for the cluster mass profile, rather than deducing and constraining it directly from the data. Various SL modelling methods have developed over the past two decades in response to the huge improvements in astronomical imaging. Most methods can be classified as 'parametric' if based on model prescriptions, or 'non-parametric' if 'grid-based' or interpolative, capable of arbitrary forms (e.g. Saha & Williams 1997; Abdelsalam, Saha & Williams 1998; Diego et al. 2005; Liesenborgs, De Rijcke & Dejonghe 2006; Valls-Gabaud et al. 2006; see also section 4.4 in Coe et al. 2008). The non-parametric grid methods do not have the resolution to accurately locate and reproduce multiple images, and usually rely on images identified by other means – often just eyeball candidates or those identified from the subset of parametric models with predictive power to locate images, for which the number of free parameters does not exceed the number of independent multiple images used as constraints.

The method developed by Broadhurst et al. (2005b), and simplified further by Zitrin et al. (2009b), has securely identified tens of multiple images in high-quality Advanced Camera for Surveys (ACS) images, behind Abell 1689 and Cl0024+1654 and also a sample of 12 MACS clusters at $z > 0.5$ sample (Zitrin et al. 2010), with only six free parameters so that in practice the number of multiple images uncovered readily exceeds the number of free parameters, as minimally required in order to get a reliable fit. This approach to SL is based on the assumption that mass approximately traces light, and will be employed here as our parametric analysis of Abell 1703. We also apply the non-parametric technique of Liesenborgs et al. (2006, 2007, 2009) which employs an adaptive grid inversion technique and has been well tested on available multiple-imaging data such as the many sets of multiple images uncovered by Zitrin et al. (2009b; with photometric redshifts calculated therein), in Cl0024+1654 (see also Liesenborgs et al. 2008).

Here we compare in more detail these two very different methods applied to Abell 1703, allowing in principle a test of the assumptions behind the parametric technique. Abell 1703 has been subject to various complementary studies ranging from early X-ray and optical work to more recent high-quality lensing analyses from ground and space (Leir & Van Den Bergh 1977; Kowalski et al. 1984; Bade et al. 1998; Cooray et al. 1998; Böhringer et al. 2000; Koester et al. 2007; Stott et al. 2007; Bruursema et al. 2008; Riley et al. 2008, 2009; Oguri et al. 2009), with detailed radio sources (Rizza et al. 2003; Coble et al. 2007) and highly magnified high-z galaxies (Zheng et al. 2009). SL analyses of Abell 1703 have been carried out by Hennawi et al. (2008), Limousin et al. (2008), de Xivry & Marshall (2009), Oguri et al. (2009), Richard et al. (2009) and Saha & Read (2009).

The cluster Abell 1703 (Abell 1958; see also Abell, Corwin & Olowin 1989) is known to have many sets of multiple images with impressive spectroscopic redshift information (Limousin et al. 2008; Richard et al. 2009; see also Estrada et al. 2007; Hennawi et al. 2008). Here we take advantage of two independent SL modelling techniques which are interesting to compare given their very different approaches. We then add the accurate WL data from Broadhurst et al. (2008; see also Medezinski et al. 2010) to complete the mass profile for comparison with theoretical predictions out to the virial radius and beyond and to examine the consistency of the WL- and SL-derived profiles in the region of overlap.

This paper is organized as follows: in Section 2 we describe the observations. In Section 3, we detail the SL modelling methods and their implementation. In Section 4 we report and discuss the results, which are then summarized in Section 5. Throughout this paper we adopt a concordance ΛCDM cosmology with ($\Omega_{\rm m0} = 0.3,\ \Omega_{\Lambda 0} = 0.7,\ h = 0.7$). We adopt a redshift of $z = 0.28$ for the cluster, equal to that of the prominent central BCG galaxy (Allen et al. 1992). With these parameters 1 arcsec corresponds to a physical scale of 4.25 kpc for this cluster. The reference centre of our analysis is fixed at the centre of the BCG: RA = 13:15:05.24, Dec. = +51:49:02.6 (J2000.0).

2 OBSERVATIONS

Abell 1703 was observed in 2004 November, with the Wide Field Channel (WFC) of the ACS installed on the *HST*, in the framework of the ACS Guaranteed Time Observations (GTO; Ford et al. 2003) which includes deep observations of several massive, intermediate-redshift galaxy clusters. Integration times of 7050, 5564, 5564, 8494+1340, 5564 × 2 and 8900 × 2 s were obtained through the F435W, F475W, F555W, F625W, F775W and F850LP filters, respectively, and are available in the Hubble Legacy Archive. Some important aims of the GTO programme are determination of the mass distribution of clusters for testing the standard cosmological model and to study distant, background lensed galaxies for which some of the very highest redshift galaxies are known because of high magnification by massive clusters (Franx et al. 1997; Frye & Broadhurst 1998; Frye, Broadhurst & Benítez 2002; Kneib et al. 2004; Stark et al. 2007; Bradley et al. 2008; Bouwens et al. 2009, in Abell 1703: Zheng et al. 2009).

As part of the ACS GTO cluster programme, in 2010 April we also observed Abell 1703 with the near-infrared channel of the *HST* new Wide Field Camera 3 [WFC3/infrared (IR)]. The observations consisted of one orbit (2812 s) each in the F125W and F160W bands.

Various redshifts have been quoted for Abell 1703 (e.g. Struble & Rood 1987, 1999; Böhringer et al. 2000), corresponding to several different cluster galaxies, out of which we adopt that of the prominent brightest cluster galaxy at $z = 0.28$ (Allen et al. 1992). This redshift was also used in recent SL work on this cluster by Limousin et al. (2008) and Richard et al. (2009) who identified many sets of multiple images which we incorporate in this work, as will be detailed below.

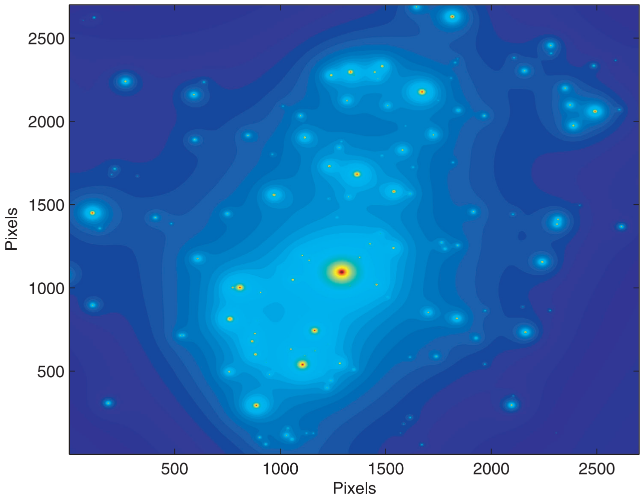

Figure 1. The starting point of the parametric model, where we define the surface mass distribution based on the cluster member galaxies (see Section 3). Axes are in ACS pixels (0.05 arcsec pixel^{-1}). North is up, east is towards left-hand side.

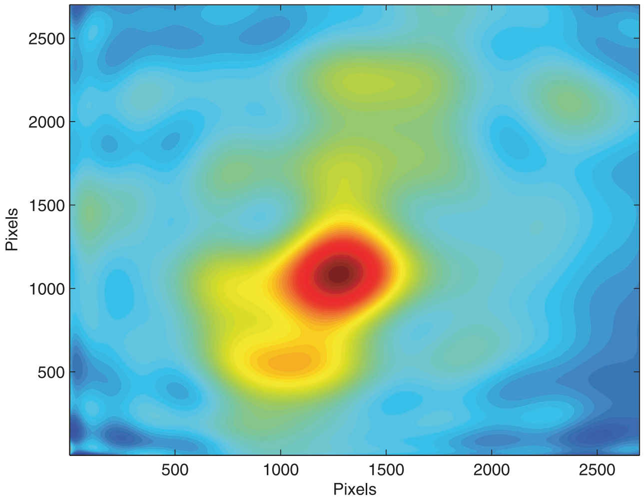

Figure 2. The resulting smooth mass component of the parametric model (see Section 3). Axes are in ACS pixels (0.05 arcsec pixel^{-1}). North is up, east is towards left-hand side.

3 STRONG-LENSING MODELLING AND ANALYSES

3.1 Parametric method

We first apply our well-tested approach to lens modelling, which has previously uncovered large numbers of multiply-lensed galaxies in ACS images of Abell 1689, Cl0024+1654, and 12 high-z MACS clusters (respectively, Broadhurst et al. 2005b; Zitrin & Broadhurst 2009; Zitrin et al. 2009a,b, 2010). The full details of this approach can be found in these earlier papers. Briefly, the basic assumption adopted is that mass approximately traces light, so that the photometry of the red cluster member galaxies is used as the starting point for our model. Cluster member galaxies are identified as lying close to the cluster sequence by the photometry provided in the Hubble Legacy Archive.

We approximate the large-scale distribution of cluster mass by assigning a power-law mass profile to each galaxy (see Fig. 1), the sum of which is then smoothed (see Fig. 2). The degree of smoothing (S) and the index of the power law (q) are the most important free parameters determining the mass profile. A worthwhile improvement in fitting the location of the lensed images is generally found by expanding to first order the gravitational potential of this smooth component, equivalent to a coherent shear describing the overall matter ellipticity, where the direction of the shear and its amplitude are free parameters, allowing for some flexibility in the relation between the distribution of DM and the distribution of galaxies, which cannot be expected to trace each other in detail. The total deflection field $\boldsymbol{\alpha}_{\mathrm{T}}(\boldsymbol{\theta})$ consists of the galaxy component, $\boldsymbol{\alpha}_{\mathrm{gal}}(\boldsymbol{\theta})$, scaled by a factor K_{gal}, the cluster DM component $\boldsymbol{\alpha}_{\mathrm{DM}}(\boldsymbol{\theta})$, scaled by $(1- K_{\mathrm{gal}})$, and the external shear component $\boldsymbol{\alpha}_{\mathrm{ex}}(\boldsymbol{\theta})$:

$$\boldsymbol{\alpha}_{\mathrm{T}}(\boldsymbol{\theta}) = K_{\mathrm{gal}}\boldsymbol{\alpha}_{\mathrm{gal}}(\boldsymbol{\theta}) + (1 - K_{\mathrm{gal}})\boldsymbol{\alpha}_{\mathrm{DM}}(\boldsymbol{\theta}) + \boldsymbol{\alpha}_{\mathrm{ex}}(\boldsymbol{\theta}), \tag{1}$$

where the deflection field at position $\boldsymbol{\theta}_m$ due to the external shear, $\boldsymbol{\alpha}_{\mathrm{ex}}(\boldsymbol{\theta}_m) = (\alpha_{\mathrm{ex},x}, \alpha_{\mathrm{ex},y})$, is given by

$$\alpha_{\mathrm{ex},x}(\boldsymbol{\theta}_m) = |\gamma| \cos(2\phi_\gamma)\Delta x_m + |\gamma| \sin(2\phi_\gamma)\Delta y_m, \tag{2}$$

$$\alpha_{\mathrm{ex},y}(\boldsymbol{\theta}_m) = |\gamma| \sin(2\phi_\gamma)\Delta x_m - |\gamma| \cos(2\phi_\gamma)\Delta y_m, \tag{3}$$

where $(\Delta x_m, \Delta y_m)$ is the displacement vector of the position $\boldsymbol{\theta}_m$ with respect to a fiducial reference position, which we take as the lower-left pixel position (1, 1), and ϕ_γ is the position angle of the spin-2 external gravitational shear measured anticlockwise from the x-axis. The normalization of the model and the relative scaling of the smooth DM component versus the galaxy contribution bring the total number of free parameters in the model to 6. This approach to SL is sufficient to accurately predict the locations and internal structure of multiple images, since in practice the number of multiple images uncovered readily exceeds the number of free parameters thus fully constraining them.

In addition, two of the six free parameters can be primarily set to reasonable values so only four of these parameters have to be constrained initially, which sets a very reliable starting point using obvious systems. The mass distribution is therefore primarily well constrained, uncovering many multiple images which can then be iteratively incorporated into the model, by using their redshift estimation and location in the image plane.

First, we use this preliminary model to lens the more obvious lensed galaxies back to the source plane by subtracting the derived deflection field and then relens the source plane to predict the detailed appearance and location of additional counter images, which may then be identified in the data by morphology, internal structure and colour. We stress that multiple images found this way must be accurately reproduced by our model and are not simply eyeball ‘candidates’ requiring redshift verification. In Abell 1703, many multiple images (16 systems, most of them with spectroscopic redshifts; Limousin et al. 2008; Richard et al. 2009) are already known and therefore simply used to constrain the fit, which is assessed by the rms uncertainty in the image plane:

$$\mathrm{rms}^2_{\mathrm{images}} = \sum_{\mathrm{i}} \left[(x'_{\mathrm{i}} - x_{\mathrm{i}})^2 + (y'_{\mathrm{i}} - y_{\mathrm{i}})^2\right] / N_{\mathrm{images}}, \tag{4}$$

where x'_{i} and y'_{i} are the locations given by the model, and x_{i} and y_{i} are the real images location, and the sum is overall N_{images} images. The best-fitting solution is unique in this context, and the model uncertainty is determined by the location of predicted images in the image plane. Importantly, this image-plane minimization does not suffer from the well-known bias involved with source-plane minimization, where solutions are biased by minimal scatter towards shallow mass profiles with correspondingly higher magnification.

The model is successively refined as additional sets of multiple images are incorporated to improve the fit, using also their redshift measurements or estimates, for better constraining the mass slope through the cosmological relation of the $D_{\mathrm{ls}}/D_{\mathrm{s}}$ growth.

3.2 Non-parametric inversion method

3.2.1 Genetic algorithm-based inversion

The non-parametric inversion method that we apply here is based on the work of Liesenborgs et al. (2006). It requires the user to specify a square-shaped region in which the inversion routine should try to reconstruct the mass distribution. Additionally, it is necessary to define which images correspond to the same source and at what redshifts the sources are located. In a first step, the square region is subdivided in a uniform way into a number of smaller square grid cells, and to each cell a projected Plummer sphere (Plummer 1911) is assigned. The width of each basis function is set proportional to the grid cell size. As an additional basis function, a sheet of mass can be included; this can be useful as in the centre of clusters a non-negligible density offset may be present which can prove difficult to model using Plummer basis functions. A genetic algorithm is then used to search for appropriate weights of these basis functions, yielding a first approximation of the projected density of the lens.

Using this first approximate solution, a new grid is then constructed in which regions containing more mass are subdivided further. It should be noted that the mass sheet basis function is not taken into consideration in this step as it is structureless. Using this new grid, basis functions are assigned and the genetic algorithm again looks for appropriate weights. This refinement procedure can be repeated until the added resolution no longer results in an improved fit to the data.

The actual search for appropriate weights of the basis functions and thus for the mass distribution employs a genetic algorithm. This is a heuristic optimization strategy, inspired by the theory of evolution by Darwin. In essence, one tries to breed solutions to a problem, by evolving an initial population of trial solutions towards solutions which are better adapted to the problem under study. To create the next generation from the current one, trial solutions are combined and mutated while applying selection pressure, i.e. making sure that solutions which are deemed better create more offspring. In this approach, it is even possible to simultaneously optimize against several so-called fitness measures; one then speaks of a multi-objective genetic algorithm (see e.g. Deb 2001).

As the number of basis functions used can become quite large (e.g. $\sim$1000) and the genetic algorithm starts from random initial solutions, several runs of this procedure will produce results that differ somewhat. Therefore a set of solutions is usually generated, so that one can inspect the common features of these mass maps, and the standard deviation can be used as a measure of the reliability at any location. The algorithm details and original fitness criteria are described in Liesenborgs et al. (2006, 2007, 2009). Below, the fitness criteria used in this work shall be described. It is based on these criteria that selection pressure will be applied.

3.2.2 Fitness criteria

In strong lens inversion one tries to deduce the projected mass distributions based on data of multiply-imaged sources. Since each set of images originates from a single source, projecting the images back on to the corresponding source plane should produce a consistent source. Previously, only extended images could be used, in which case the back-projected images should overlap in the source plane. To calculate the amount of overlap, the estimated size of the source was used as a length-scale. The method was adapted to work with point images as well. In this case, the envelope of all estimated source positions is used as a length-scale when calculating the distances between the back-projected images of each source. Using this length-scale instead of an absolute scale prevents scaling the source plane to obtain a better fitness value. This is especially important when a mass sheet is included as a basis function since it has precisely this effect.

Apart from the locations where images can be seen, additional constraints come from the area in which no images are observed, i.e. the null space. To avoid predicting extra images, which corresponds to avoiding unnecessary substructure, the user can define a region which will be used to check for additional images. This region is divided into a large number of triangles, and for each source the triangles are projected on to the source plane. Each triangle that overlaps with the envelope of the back-projected images is counted and the total count for all sources is used as the null-space fitness measure. As for each source this gives an approximation of the amount of images, a lower value indicates a better fitness with respect to this criterion.

3.2.3 Input

The input of the inversion routine consists of multiply-imaged systems together with their redshifts. The systems listed in Richard et al. (2009) were used for this purpose, and where available spectroscopic redshift information was used. For Systems 2, 8, 9 and 12, the redshift predicted by the model in this work was used, as these redshifts were in good agreement with the photometric ones. Note, Systems 13 and 14 were not used in the inversion as the redshift estimates seemed more uncertain (however, we do find that including them results only in minor changes to the mass model). Based on these image systems, the inversion routine was instructed to look for mass in a 2 × 2 arcmin^2 region, roughly centred on the cD galaxy. To limit the amount of predicted images that were not part of the input, and therefore to limit the amount of unnecessary substructure, the null-space region was 3 × 3 arcmin^2 in size and a 48 × 48 grid was used for calculating the corresponding fitness measure.

4 RESULTS AND DISCUSSION

4.1 Strong-lensing regime and cD galaxy

In the SL regime, we have modelled Abell 1703 (see Fig. 3) using the many sets of multiply-lensed images previously identified, most of which have spectroscopic redshifts reported in Limousin et al. (2008) and Richard et al. (2009). Here we also incorporate the new WFC3/IR imaging, which reveals the distinct colours of each system and enables the identification of an additional system (17) following the same symmetry as Systems 15/16 (see Figs 4 and 5) with a similar model redshift of $z_{\mathrm{s}} \sim 2.8$. We have used the parametric method of Zitrin et al. (2009b) to further verify the reliability of the many multiply-lensed images across the field and to securely input them into the non-parametric method of Liesenborgs et al. (2006) to model the central mass distribution.

Our parametric model (see Fig. 6) accurately reproduces all multiply-lensed images, indicating that our preliminary assumption that mass traces light is reasonable. In order to further test this assumption, we then applied the non-parametric technique of Liesenborgs et al. (2006, 2007, 2009) for which no

Figure 3. Galaxy cluster Abell 1703 ($z = 0.28$) imaged with the Hubble/ACS. The overlaid critical curve (blue) corresponds to the distance of System 1, at $z_s = 0.889$. The outer white critical curve corresponds to the giant arc (Systems 10/11) at higher redshift, $z_s = 2.627$, enclosing a critical area of an effective Einstein radius of $\simeq$130 kpc at the redshift of this cluster. North is up, east is towards left-hand side.

prior information for the distribution of cluster galaxies or mass is input. Nevertheless, the results of this method seem to trace the distribution of light as can be seen in Fig. 7, generating a two-dimensional (2D) mass distribution which is remarkably similar to the result of the parametric mass model on the large scale, shown in Fig. 6. A distinct substructure is seen in both maps and corresponds to local galaxy overdensities. In addition, the two methods produce very similar mass profiles over a range of scales covering the full distribution of multiple images, with a mean inner slope of $\mathrm{d}\log\Sigma/\mathrm{d}\log\theta \simeq -0.5$.

We have examined the difference between these two mass maps by subtracting the non-parametric mass distribution from the parametric mass distribution. The result is shown in Fig. 8. As can be seen in this figure, the main positive differences, marked in red, occur mainly where galaxies are located in the data, since these must contain mass and are included only in the parametric model. The non-parametric model does place mass at these locations, but it is usually smoothly distributed as this approach to modelling does not make prior assumptions about the mass distribution and thus does not achieve a spatial resolution sufficient for resolving individual cluster galaxies. The main negative differences, marked in blue, are seen where the non-parametric model has more mass than implied by the galaxy distribution, but overall these are small and likely inevitable given the inherent noise set by the finite amount of input data. The mean difference across this field is $|\Delta\kappa| = 0.19$, contributed mainly by the inclusion of cluster members or discrepancies outside the critical curves, where one has relatively poor constraints from the observed multiple images.

The parametric method of Zitrin et al. (2009b) has been shown to have the predictive power to find many multiple images in the field. This parametric method has inherently more structure on small scales by virtue of the inclusion of cluster members which can significantly deflect images locally and must be included in order to find lensed images. Due to the low number of parameters this model is initially well constrained using only a few sets of usually obvious multiple systems, thus correlated to the initial mass distribution so that the image-plane reproduction accuracy can be only somewhat improved as newly found multiple systems are incorporated, but the overall gradient of the cluster lensing profile is significantly refined through the cosmological distance–redshift relation. It is important to have a wide range of background source redshifts for a reliable profile determination, otherwise the SL models are

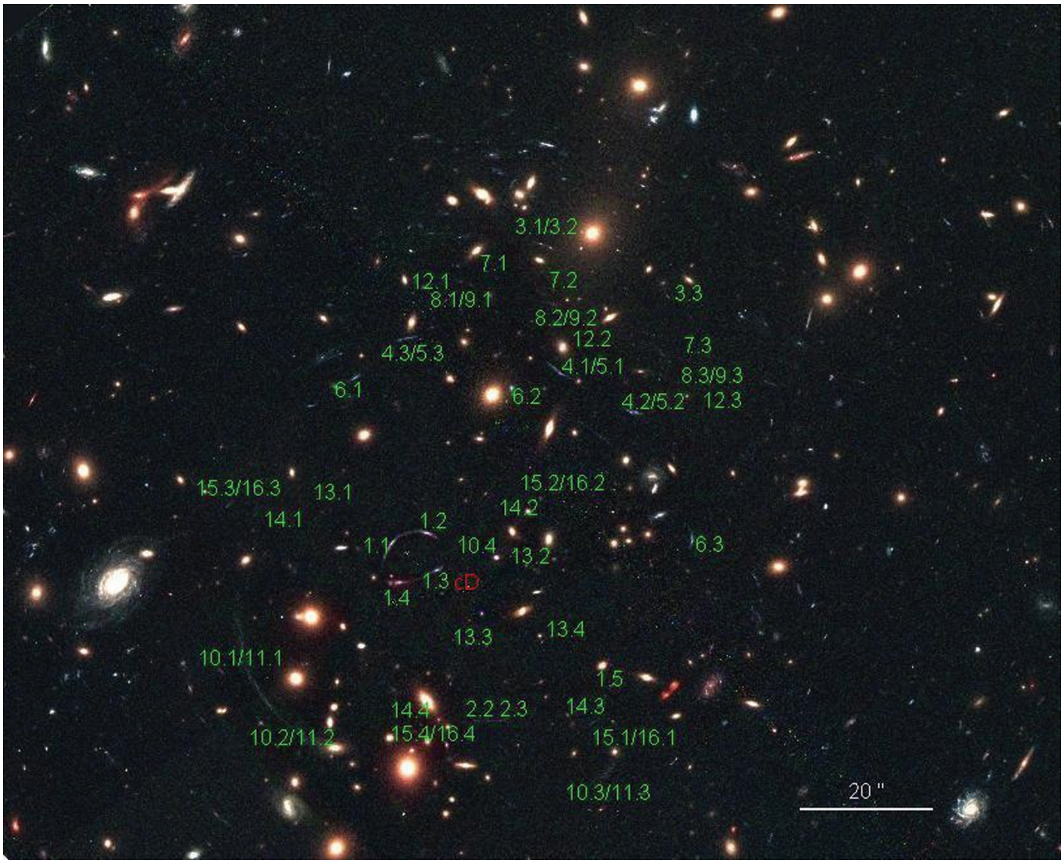

Figure 4. Distribution of multiply-lensed images used to constrain the models marked on a colourful Hubble/ACS image of Abell 1703, with some central galaxies including the cD galaxy subtracted, and its original location marked in red. Subtraction has been carried out by modelling the main cD galaxy and three other galaxies using Chebyshev–Fourier basis functions ('CheF-lets'; Jiménez-Teja & Benítez, in preparation). These multiply-lensed images and more details can be found in Limousin et al. (2008) and Richard et al. (2009). North is up, east is towards left-hand side.

degenerate with respect to the profile, although the relative distribution of matter and substructure can still be reasonable, finding many sets of multiple images. In the non-parametric approach on the other hand, the fit is much more flexible and is continuously improved as more of these images are incorporated and the overall solution is clarified, allowing the exclusion of a wide range of non-unique solutions (Liesenborgs et al. 2006, 2008). When sufficient images are incorporated, the overall mass distributions and profiles of these two methods become very similar, as we have found here and are shown in the comparison of Figs 6–8.

The critical curves for different sources are plotted on the cluster image in Fig. 3. The critical curves for a source redshift of $z_{\rm s} = 2.627$ enclose an area with an effective Einstein radius of 30.5 ± 3 arcsec ($\simeq$130 kpc at the redshift of the cluster) and a mass of $1.25 \pm 0.1 \times 10^{14}\,{\rm M}_{\odot}$. Our parametric model reproduces all multiply-lensed systems within a $\sigma_{\rm i} = 1.5$ arcsec of their real location. In particular, our best-fitting parametric model accurately reproduces the complicated ring ($z_{\rm s} = 0.889$; System 1) as can be seen in Fig. 9. We note that only models with central mass profiles steeper than a certain threshold accurately reproduce all parts of the ring, importantly enabling us to constrain the mass and the profile of the cD galaxy in the range $\simeq$1–5 arcsec, where the closest image of the ring system forms. This is also shown in Fig. 10.

We find that the cD galaxy encloses a *projected* mass of $5.2 \pm 0.4 \times 10^{11}\,{\rm M}_{\odot}$ within a radius of $\simeq$5 arcsec ($\simeq$22 kpc) after subtracting the interpolated smooth DM component ($\simeq 6.3 \times 10^{12}\,{\rm M}_{\odot}$ inside this aperture) and has a B-band luminosity of $8.8 \pm 0.1 \times 10^{10} L_{\odot}$ [fluxes were converted to luminosities using the luminous red galaxies (LRG) template described in Benítez et al. 2009]. This corresponds to an averaged M/L_B of $\sim$6 $(M/L)_{\odot}$ in this region. This ratio can be fully accounted for by the stars contained in this galaxy, for which we obtain as well $M/L_B \simeq 6\ (M/L)_{\odot}$, for a single-burst stellar population formed at $z = 3$ and viewed at a redshift of $z = 0.28$, equivalent to an age of $\simeq$8.1 Gyr, and with half solar metallicity (by evolutionary models of Bruzual & Charlot 2003). This result is in agreement with the result of Limousin et al. (2008) and is similar to other lensing-based cD masses in well-studied clusters, for which low M/L ratios are also found and fully accounted for by the measured stellar light (e.g. Gavazzi et al. 2003 for MS2137-2353 and Zitrin & Broadhurst 2009 for MACS J1149.5+2223).

We mentioned in the preceding sections that the profile can only be accurately constrained by incorporating the cosmological redshift–distance relation, i.e. the lensing distance of each system based on the measured spectroscopic redshifts. In doing so we make use in particular of the $z = 0.889$ system (the ring; System number 1), whose redshift is very distinct from the rest of the multiple-image systems, thus strongly constraining the profile. We examine how well the cosmological relation is reproduced by the parametric model, accounting also for all other systems with reliable spec-z measurements, as shown in Fig. 11. Clearly the redshifts of these

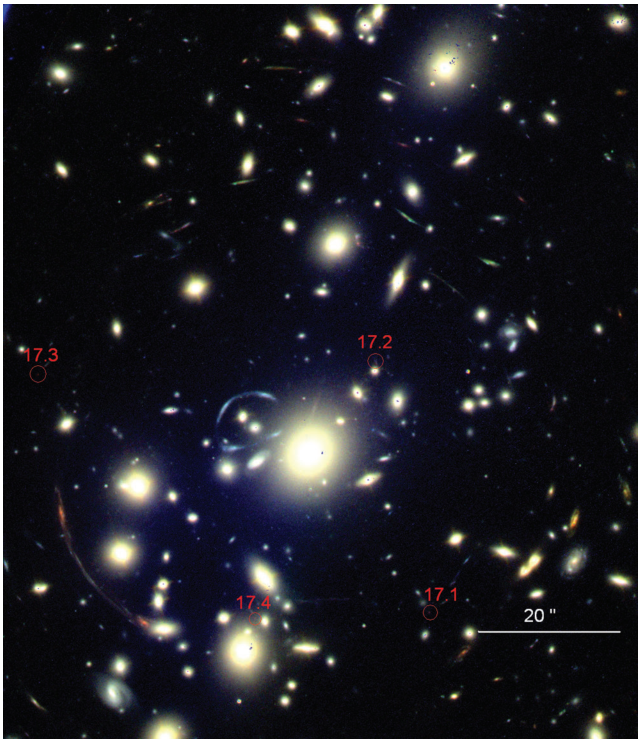

Figure 5. An optical/ACS + IR/WFC3 colourful image of the central region of Abell 1703. The much wider colour range enabled by incorporation of the IR data manifests the distinct colours of the many multiple systems shown in Figs 3 and 4, and the identification of an additional system (17) marked in circles, following the same symmetry of Systems 15 and 16 (Fig. 4).

systems verify very well that the predicted deflection of the best-fitting model at the redshift of each of these systems lies precisely along the expected cosmological relation, with a mean deviation of only $\Delta_f < 0.01$ (see Fig. 11), and $\chi^2 = 0.1$ for the best model, considerably strengthening the plausibility of our parametric approach to modelling in general. In Figs 12–14 we give further examples demonstrating how different systems are accurately reproduced by our parametric model, in addition to the remarkable reproduction of the ring system seen in Fig. 9.

4.2 Combined weak and strong lensing

We now compare our SL analysis results with undiluted WL data from deep *Subaru* $g'r'i'$ images (Broadhurst et al. 2008). The *Subaru* WL data, covering a wide field of $\approx 34 \times 27$ arcmin^2, allow us to probe the cluster mass distribution over a wide radial range, $\theta \approx [0.7\,\text{arcmin}, 18\,\text{arcmin}]$, in the subcritical regime ($\theta >$ 30 arcsec).

For a direct comparison with the WL data, we followed the method outlined in Umetsu et al. (2010) to translate our SL mass profiles into corresponding tangential distortion profiles $g_+(\theta) = \gamma_+(\theta)/[1 - \kappa(\theta)]$ for a fiducial source redshift $z_s = 1$, roughly matching the mean depth of blue+red background galaxies used for the WL analysis. In Fig. 15, we compare our parametric and non-parametric SL inner profiles with the *Subaru* distortion profile. Our SL and WL results are in good agreement where the data overlap, $\theta = [40\,\text{arcsec}, 90\,\text{arcsec}]$, for both SL methods. Furthermore, a simple inward extrapolation of the best-fitting NFW profile (see Table 1) for the outer *Subaru* observations with input of the Einstein radius fits well with the inner SL information, in particular, slightly better for the non-parametric profile. The parametric profile has a minor 'bump' around ~30 arcsec due to other bright galaxies in the field that are not included in the non-parametric model. This translates into a dip in the $g_+(\theta)$ profile of the parametric technique, slightly deviating from the smooth NFW curve. Furthermore, the WL+Einstein radius NFW fitting assumes a circularly symmetric lens, possibly biasing this NFW profile fit done this way.

We then reconstruct the outer mass profile from the *Subaru* WL data using the shear-based 1D inversion method outlined in Umetsu et al. (2009, 2010). Fig. 16 compares our SL and WL results in terms of the lens convergence profile, $\kappa(\theta)$, where the combined SL and WL results produce a coherent mass profile with a continuously steepening radial trend from the central region to the outskirts of the cluster.

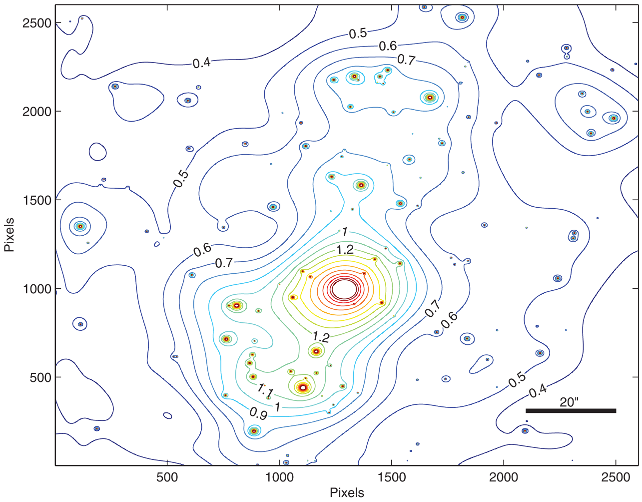

Figure 6. 2D surface mass distribution (κ), in units of the critical density (for $z_s = 2.627$), of Abell 1703. Contours are shown in linear units, derived from the parametric mass model constrained using the many sets of multiply-lensed images seen in Fig. 4. Axes are in ACS pixels (0.05 arcsec pixel^{-1}). North is up, east is towards left-hand side.

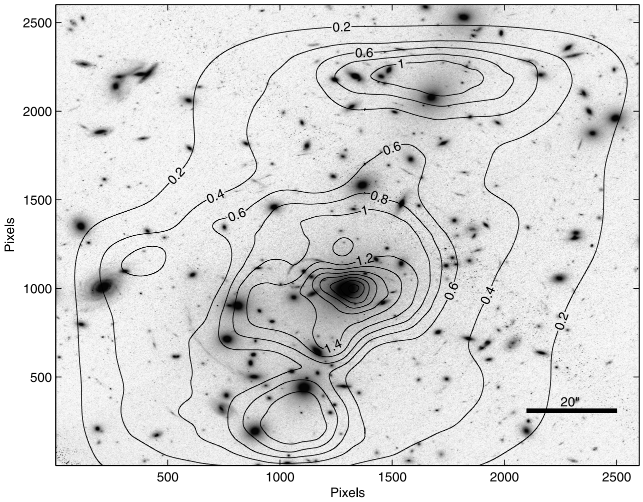

Figure 7. 2D surface mass distribution (κ) contours overlaid on the cluster image, derived from the non-parametric mass model constrained using the multiply-lensed images seen in Fig. 4. As can be seen, though no galaxies were included in this modelling method, the mass contours steepen up where significant galaxies are present. Clearly this mass distribution is in good agreement with the parametric mass distribution seen in Fig. 6.

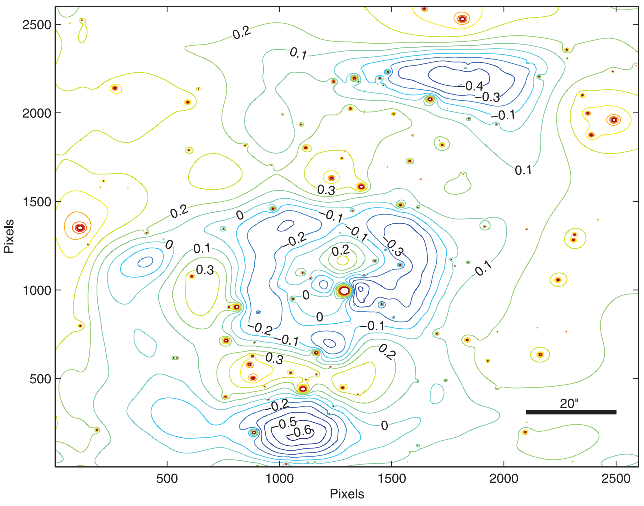

Figure 8. A 2D contour map of the difference between the parametric (Fig. 6) and the non-parametric (Fig. 7) mass distributions. Contours are in $\Delta\kappa$, plotted in equal linear spaces of 0.1. The main positive differences (red) are seen where galaxies are located in the data (since these are included only in the parametric model), and the main negative differences (blue) are seen where the non-parametric model has more mass than implied by the galaxy distribution. Still these differences are overall small, with a mean difference of $|\Delta\kappa| = 0.19$ across this field, contributed mainly by the inclusion of cluster members or discrepancies outside the critical curves, where one has relatively poor constraints from the observed multiple images.

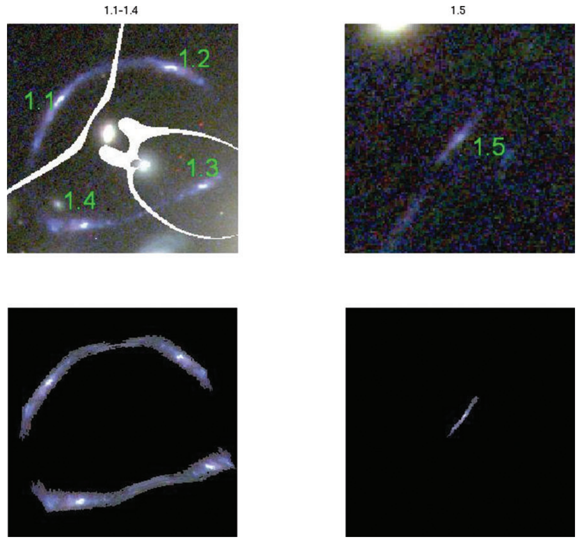

Figure 9. Reproduction of System 1 by our model, by delensing image 1.4 into the source plane, and then relensing the source-plane pixels on to the image plane to accurately form the ring. By tuning the inner slope of the mass distribution, the observed structure is reproduced very closely. A small fifth image, 1.5, is formed outside the tangential critical curve (for $z_s = 0.889$; see Figs 3 and 4).

Overall, we combine our SL and WL results to examine the form of the underlying cluster mass profile and to characterize cluster mass and structure properties. To do this, we fit our SL and WL constraints with an NFW profile in four independent manners: first, we fit the *Subaru* distortion profile $g_+(\theta)$ alone with no SL information involved. Secondly, we utilize the inner Einstein radius constraint, $\theta_E = 30.5 \pm 3$ arcsec (10 per cent uncertainty) at $z_s = 2.627$, in conjunction with the *Subaru* distortion profile (for details, see Umetsu & Broadhurst 2008 and Umetsu et al. 2010). Most credibly, we then fit our joint SL+WL convergence profiles $\kappa(\theta)$ of the parametric and non-parametric SL methods following the prescription given by Umetsu et al. (2010). For the joint NFW fitting, we constrain the SL data to the range [5 arcsec, 25 arcsec] where the two independent SL profiles are extremely similar, and since in general the shapes of the SL mass profiles within the Einstein radius look smoother, matching the expectation from the outer WL profile

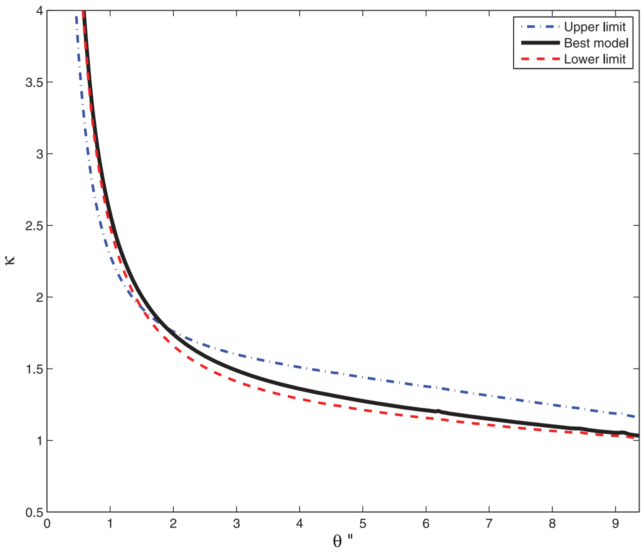

Figure 10. The four images of the ring (System 1, $z_s = 0.889$; see also Fig. 9) next to the cluster core enable a unique determination of the cD galaxy mass profile in the range $\simeq$1–5 arcsec (i.e. $\simeq$4–22 kpc; where the closest image of the ring appears). The solid thick black line represents the best-fitting parametric model which accurately reproduces the ring. The dashed red line represents the minimum 'shallowness' threshold, meaning that only models higher than this threshold will form the four images of the ring, and the dash–dotted blue line shows the limit above which these images become overly distorted.

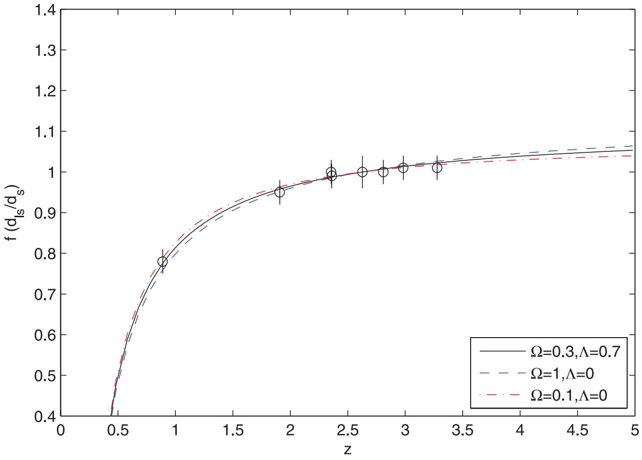

Figure 11. Growth of the scaling factor $f(d_{ls}/d_s)$ as a function of redshift, normalized so $f = 1$ at $z = 2.627$. Plotted lines are the expected ratio from the chosen specified cosmological model. The circles correspond to the multiple-image systems reproduced by the parametric mass model versus their real spectroscopic redshift. The data follow very well the relation predicted by the standard cosmological model (mean deviation of only $\Delta_f < 0.01$, and $\chi^2 = 0.1$ for this fit).

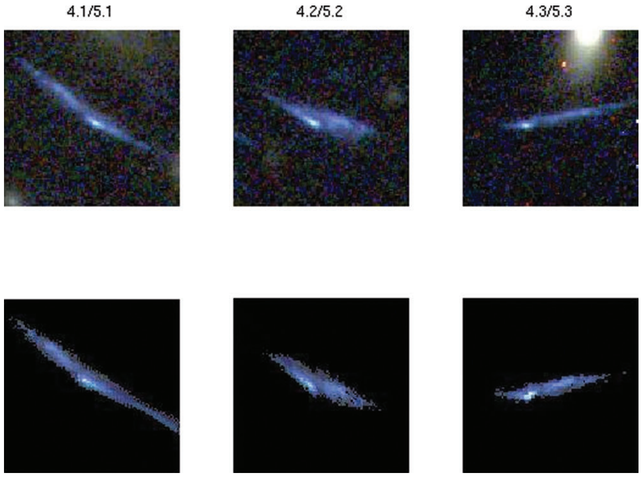

Figure 12. Reproduction of Systems 4 and 5 by our model, by delensing image 4.1/5.1 into the source plane, and relensing the source-plane pixels on to the image plane to accurately form the other images of this system.

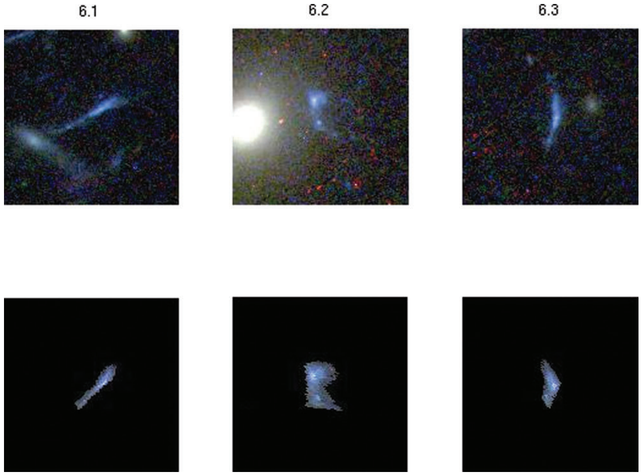

Figure 13. Reproduction of System 6 by our model, by delensing image 6.2 into the source plane, and relensing the source-plane pixels on to the image plane to accurately form the resolved internal details of the other images of this system.

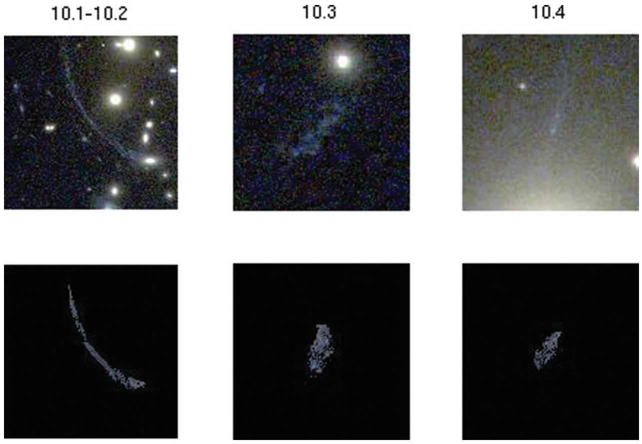

Figure 14. Reproduction of the giant arc, Systems 10 and 11, by our model. We delens image 10.2 into the source plane, and relens the source-plane pixels on to the image plane, which accurately also reproduces the other half of the main arc, image 10.1, and two other smaller images (10.3 and 10.4; see Figs 3 and 4).

better. All these methods yield similar and consistent results, which are also summarized in Table 1.

The NFW universal density profile has a two-parameter functional form as (Navarro, Frenk & White 1997)

$$\rho_{\rm NFW}(r) = \frac{\rho_{\rm s}}{(r/r_{\rm s})(1+r/r_{\rm s})^2}, \tag{5}$$

where $\rho_{\rm s}$ is a characteristic inner density and $r_{\rm s}$ is a characteristic inner radius. The logarithmic gradient $n \equiv {\rm d}\ln\rho(r)/{\rm d}\ln r$ of the NFW density profile flattens continuously towards the centre of mass, with a flatter central slope $n = -1$ and a steeper outer slope ($n \to -3$ when $r \to \infty$) than a purely isothermal structure ($n = -2$). A useful index, the concentration, compares the virial radius, $r_{\rm vir}$, to $r_{\rm s}$ of the NFW profile, $c_{\rm vir} = r_{\rm vir}/r_{\rm s}$.

We specify the NFW model with the halo virial mass $M_{\rm vir}$ and the concentration $c_{\rm vir}$ instead of $\rho_{\rm s}$ and $r_{\rm s}$. Here the errors for these best-fitting NFW parameters include the uncertainty in the source redshift calibration for WL, $\bar{z}_{\rm s} = 1.0 \pm 0.2$. The typical halo concentration obtained by the four methods described above is $c_{\rm vir} \simeq 7.5 \pm 0.5$, and the typical virial mass is $M_{\rm vir} \simeq 1.2 \pm 0.15 \times 10^{15}\,{\rm M}_{\odot}\,h^{-1}(r_{\rm vir} \simeq 1.84\,{\rm Mpc}\,h^{-1})$. The joint SL+WL fits yield $c_{\rm vir} \simeq 7.15 \pm 0.5$ and $M_{\rm vir} \simeq 1.22 \pm 0.15 \times 10^{15}\,{\rm M}_{\odot}\,h^{-1}$, agreeing with the recent result of Oguri et al. (2009; $c_{\rm vir} \simeq 6.5^{+1.2}_{-0.7}$, $M_{\rm vir} \simeq 1.05^{+0.28}_{-0.25} \times 10^{15}\,{\rm M}_{\odot}\,h^{-1}$). This puts Abell 1703 above the standard *c–M* relation and manifests again the tension with the standard ΛCDM model. This can be seen in Fig. 17 where we plot confidence levels of the concentration parameter derived for Abell 1703, along with *c–M* relations including 1σ uncertainties, deduced from simulations by Duffy et al. (2008) with *Wilkinson Microwave Anisotropy Probe 5* (*WMAP*5) parameters and scaled to $z_c = 0.28$. Since the concentration parameter depends on cluster formation time (as discussed recently by Sadeh & Rephaeli 2008) and though such conclusions have previously been reached for several other massive clusters (e.g. Broadhurst et al. 2008; Umetsu et al. 2010), a similar comparison should naturally be made for many other clusters in order to clearly establish that a statistically significant trend is discerned.

5 SUMMARY

In this work, we have produced an accurate full-range profile of the cluster Abell 1703, based on combined WL and SL mass models applied to exceptionally high-quality space and ground-based imaging data, including recent observations of the WFC3/IR on the *HST*. This profile adds to the relatively few clusters for which precise and reliable mass profiles have been constructed, including MS2137 (Gavazzi et al. 2003; Merten et al. 2009), Abell 1689 (Broadhurst et al. 2005a,b; Lemze et al. 2008; Umetsu & Broadhurst 2008; Limousin et al. 2007), Abell 2218 (Kneib et al. 1996; Abdelsalam et al. 1998) and Cl0024+1654 (Zitrin et al. 2009b; Umetsu et al. 2010).

We have applied two independent SL techniques in order to derive the inner mass profile and to examine for consistency the basic assumption of the parametric model that mass traces light. Both techniques derive remarkably similar mass distributions with the same major substructure present, and with similar overall radial mass profiles (with a mean interior slope of ${\rm d}\log\Sigma/{\rm d}\log\theta \simeq -0.5$). This inner profile matches well with the WL data in the region of overlap, at around ∼200 kpc. The two SL modelling methods cannot be distinguished in terms of the radial profile or the overall large-scale

Table 1. Comparison of the different NFW parameters obtained independently by different lensing techniques. Column 1: the method; Column 2: resulting concentration parameter, $c_{\rm vir}$; Column 3: resulting virial mass, $M_{\rm vir}$, in $10^{15}\,{\rm M}_{\odot}\,h^{-1}$; Column 4: reduced χ^2 of the fit; Column 5: Q-value goodness of fit.

Method	$c_{\rm vir}$	$M_{\rm vir}$	Reduced χ^2	Q-value
WL + parametric SL	7.07 ± 0.47	$1.18^{+0.12}_{-0.11}$	0.33	0.99
WL + non-parametric SL	7.23 ± 0.45	$1.26^{+0.13}_{-0.11}$	0.43	0.99
WL alone	$7.71^{+2.22}_{-1.66}$	$1.15^{+0.28}_{-0.22}$	0.57	0.82
WL + θ_e	$7.92^{+1.34}_{-1.07}$	$1.14^{+0.23}_{-0.21}$	0.52	0.88

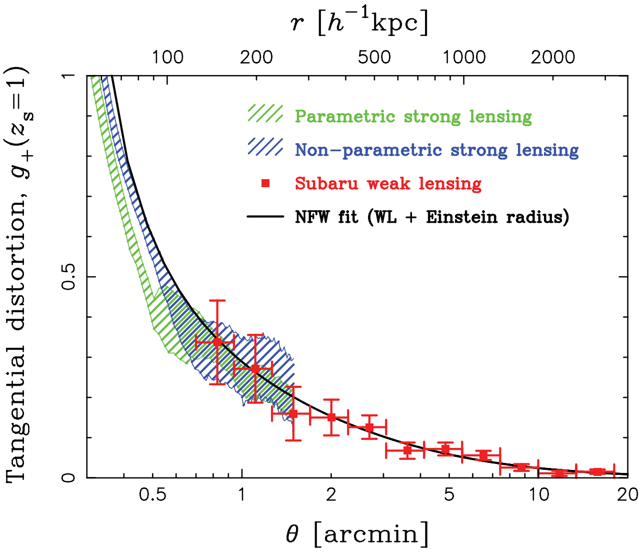

Figure 15. Comparison of our parametric and non-parametric SL profiles with the *Subaru* distortion profile. Our SL and WL results are in good agreement where the data overlap, θ = [40 arcsec, 90 arcsec], for both SL methods. Furthermore, a simple inward extrapolation of the best-fitting NFW profile (black solid curve; see also Table 1) for the outer *Subaru* observations with input of the Einstein radius fits well with the inner SL information, in particular, slightly better for the non-parametric profile. The parametric profile has a minor ‘bump’ around ∼30 arcsec due to other bright galaxies in the field which are not included in the non-parametric model, translating into a dip in the $g_+(\theta)$ profile of the parametric technique, slightly deviating from the smooth NFW curve.

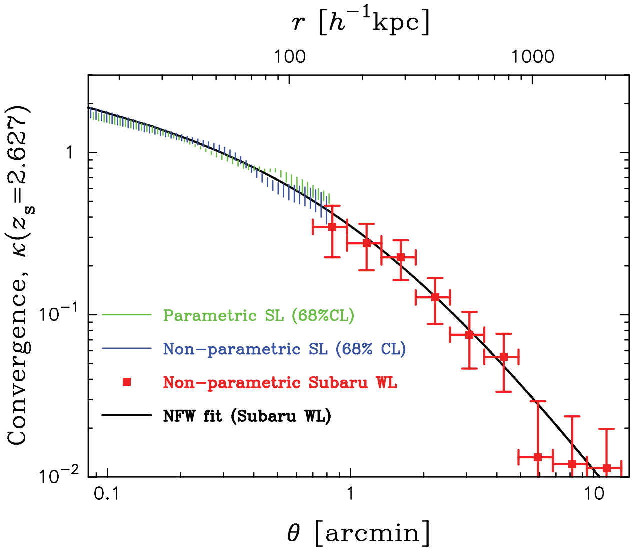

Figure 16. Comparison of our SL and WL results in terms of the lens convergence profile, $\kappa(\theta)$. The combined SL and WL results produce a coherent mass profile with a continuously steepening radial trend from the central region to the outskirts of the cluster. Both SL methods are in very good agreement with the WL data and the NFW fit (see also Table 1).

mass distribution but differ mainly on fine scales principally owing to the inclusion of cluster members in the parametric method.

Comparisons between other, different mass-modelling methods have been made before (e.g. Valls-Gabaud et al. 2006; Coe et al. 2008, 2010; Donnarumma et al. 2010; Meneghetti et al. 2010). Here we find that the galaxy contribution is important to include in order to obtain accurate predictive power, as is the case in the parametric model (Zitrin et al. 2009b, 2010) which identifies and reproduces many multiple images, even if initially constrained only by a few obvious systems. On the other hand, being correlated to the initial light distribution, the parametric model may at times be less flexible and therefore oversensitive to local luminous clumps or substructure than the non-parametric model which does not make any prior assumptions about the input distribution of mass (Liesenborgs et al. 2006).

We have made use of the reproduction ability of our parametric-model and the remarkable multiply-lensed ring-like system next to the cD galaxy to uniquely constrain its projected mass *and profile* in the inner region ≃1–5 arcsec (≃4–22 kpc). We have also found that the low M/L_B of ∼6 $(M/L)_{\odot}$ in this region can be fully accounted for by stars, similar to cD galaxies in other well-known clusters. The effect of baryons on halo density profiles is still unclear and may be related to ‘overcooling’ claimed in studies of this effect (Barkana & Loeb 2010; Duffy et al. 2010; Mead et al. 2010). Further characterization of cD galaxies from detailed lensing work will shed more light on this still poorly understood class of objects.

We have found that Abell 1703 lies above the standard c–M relation (Fig. 17), similar to several other well-known clusters for which detailed lensing-based mass profiles have been constructed, adding to the claimed tension with the standard ΛCDM model (e.g. Broadhurst et al. 2008; Umetsu et al. 2010; see also Sadeh & Rephaeli 2008). Still, the overall level of systematic uncertainties may be too large to allow a definite conclusion regarding a clear inconsistency with ΛCDM predictions. To further explore this apparent discrepancy a substantial multicycle Hubble programme has been established, based on an X-ray-selected sample of relaxed clusters so that no lensing bias is present in their selection (the CLASH programme; see also Section 1), for which the SL techniques applied here will be of great value for deriving a statistically large and unbiased measurement of the equilibrium mass profiles of galaxy clusters.

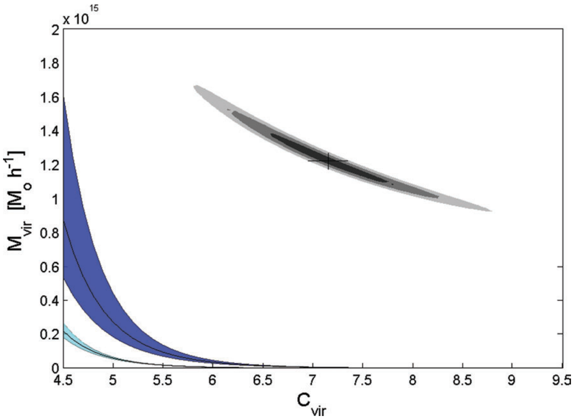

Figure 17. χ^2 confidence levels (grey-scale; 68.3, 95.4 and 99.7 per cent confidence levels) of the joint SL+WL data fits to an NFW profile of Abell 1703, presented on the *c–M* plane. Overplotted are the expected *c–M* relations and their 1σ uncertainties, presented in Duffy et al. (2008) with *WMAP*5 parameters, scaled to $z_c = 0.28$. The cyan-shaded curve corresponds to the full Duffy et al. (2008) sample, and the blue-shaded curve corresponds to their relaxed-halo sample. As can be seen Abell 1703 lies above the standard *c–M* relation.

ACKNOWLEDGMENTS

We thank Thomas Erben, the reviewer of this work, for many useful comments which improved this paper. AZ acknowledges Eran Ofek and Salman Rogers for their publicly available MATLAB scripts. This research is being supported by the Israel Science Foundation grant 1400/10. ACS was developed under NASA contract NAS 5-32865. This research is based on observations provided in the Hubble Legacy Archive which is a collaboration between the Space Telescope Science Institute (STScI/NASA), the Space Telescope European Coordinating Facility (ST-ECF/ESA) and the Canadian Astronomy Data Centre (CADC/NRC/CSA). Part of this work is based on data collected at the *Subaru* Telescope, which is operated by the National Astronomical Society of Japan.

REFERENCES

Abdelsalam H. M., Saha P., Williams L. L. R., 1998, AJ, 116, 1541
Abell G. O., 1958, ApJS, 3, 211
Abell G. O., Corwin H. G., Jr, Olowin R. P., 1989, ApJS, 70, 1
Allen S. W. et al., 1992, MNRAS, 259, 67
Bade N. et al., 1998, A&AS, 127, 145
Barkana R., Loeb A., 2010, MNRAS, 405, 1969
Benítez N. et al., 2009, ApJ, 691, 241
Böhringer H. et al., 2000, ApJS, 129, 435
Bouwens R. J. et al., 2009, ApJ, 690, 1764
Bradač M. et al., 2006, ApJ, 652, 937
Bradač M. et al., 2008, ApJ, 681, 187
Bradley L. D. et al., 2008, ApJ, 678, 647
Broadhurst T., Takada M., Umetsu K., Kong X., Arimoto N., Chiba M., Futamase T., 2005a, ApJ, 619, 143
Broadhurst T. et al., 2005b, ApJ, 621, 53
Broadhurst T., Umetsu K., Medezinski E., Oguri M., Rephaeli Y., 2008, ApJ 685, L9
Bruzual G., Charlot S., 2003, MNRAS, 344, 1000
Bruursema J., Riley S., Ford H. C., Zekser K. C., Infante L., Postman M., 2008, A&AS, 212, 1901
Coble K. et al., 2007, AJ, 134, 897
Coe D., Fuselier E., Benítez N., Broadhurst T., Frye B., Ford H., 2008, ApJ, 681, 814
Coe D., Benítez N., Broadhurst T., Moustakas L., Ford H., 2010, preprint (arXiv:1005.0398)
Cooray A. R., Grego L., Holzapfel W. L., Joy M., Carlstrom J. E., 1998, AJ, 115, 1388
Deb K., 2001, Multi-Objective Optimization Using Evolutionary Algorithms. Wiley, New York
Deb S., Goldberg D. M., Heymans C., Morandi A., 2010, preprint (arXiv:0912.4260)
de Xivry G. O., Marshall P., 2009, MNRAS, 399, 2
Diego J. M., Sandvik H. B., Protopapas P., Tegmark M., Benítez N., Broadhurst T., 2005, MNRAS, 362, 1247
Donnarumma A. et al., 2010, preprint (arXiv:1002.1625)
Duffy A. R., Schaye J., Kay S. T., Dalla Vecchia C., 2008, MNRAS, 390, 64
Duffy A. R., Schaye J., Kay S. T., Dalla Vecchia C., Battye R. A., Booth C. M., 2010, MNRAS, 405, 2161
Estrada J. et al., 2007, ApJ, 660, 1176
Ford H. C. et al., 2003, in Blades J. C., Siegmund O. H. W., eds, Proc. SPIE, Vol. 4854, Future EUV/UV and Visible Space Astrophysics Missions and Instrumentation. SPIE, Bellingham, p. 81
Franx M., Illingworth G. D., Kelson D. D., van Dokkum P. G., Tran K., 1997, ApJ, 486, 75
Frye B., Broadhurst T., 1998, ApJ, 499, 115
Frye B., Broadhurst T., Benítez N., 2002, ApJ, 568, 558
Gavazzi R., Fort B., Mellier Y., Pello R., Dantel-Fort M., 2003, A&A, 403, 11
Halkola A., Hildebrandt H., Schrabback T., Lombardi M., Bradač M., Erben T., Schneider P., Wuttke D., 2008, A&A, 481, 65
Hennawi J. F. et al., 2008, AJ, 135, 664
Horesh A., Maoz D., Ebeling H., Seidel G., Bartelmann M., 2010, MNRAS, 406, 1318
Kausch W., Schindler S., Erben T., Wambsganss J., Schwope A., 2010, A&A, 513, A8
Kneib J. P., Mellier Y., Fort B., Mathez G., 1993, A&A, 273, 367
Kneib J.-P., Ellis R. S., Smail I., Couch W. J., Sharples R. M., 1996, ApJ, 471, 643
Kneib J.-P., Ellis R. S., Santos M. R., Richard J., 2004, ApJ, 607, 697
Koester B. P. et al., 2007, ApJ, 660, 239
Kowalski M. P., Cruddace R. G., Wood K. S., Ulmer M. P., 1984, ApJS, 56, 403
Leir A. A., Van Den Bergh S., 1977, ApJS, 34, 381
Lemze D., Barkana R., Broadhurst T., Rephaeli Y., 2008, MNRAS, 386, 1092
Liesenborgs J., De Rijcke S., Dejonghe H., 2006, MNRAS, 367, 1209
Liesenborgs J., De Rijcke S., Dejonghe H., Bekaert P., 2007, MNRAS, 380, 1729
Liesenborgs J., de Rijcke S., Dejonghe H., Bekaert P., 2008, MNRAS, 389, 415
Liesenborgs J., De Rijcke S., Dejonghe H., Bekaert P., 2009, MNRAS, 397, 341
Limousin M. et al., 2007, ApJ, 668, 643
Limousin M. et al., 2008, A&A, 489, 23
Mead J. M. G., King L. J., Sijacki D., Leonard A., Puchwein E., McCarthy I. G., 2010, MNRAS, 406, 434
Medezinski E., Broadhurst T., Umetsu K., Oguri M., Rephaeli Y., Benítez N., 2010, MNRAS, 405, 257
Meneghetti M., Rasia E., Merten J., Bellagamba F., Ettori S., Mazzotta P., Dolag K., 2010, A&A, 514, A93
Merten J., Cacciato M., Meneghetti M., Mignone C., Bartelmann M., 2009, A&A, 500, 681
Navarro J. F., Frenk C. S., White S. D. M., 1996, ApJ, 462, 563 (NFW)
Navarro J. F., Frenk C. S., White S. D. M., 1997, ApJ, 490, 493 (NFW)
Newman A. B. et al., 2009, ApJ, 706, 1078
Oguri M. et al., 2009, ApJ, 699, 1038
Okabe N., Takada M., Umetsu K., Futamase T., Smith G. P., 2010, PASJ, 62, 811
Plummer H. C., 1911, MNRAS, 71, 460

Richard J., Pei L., Limousin M., Jullo E., Kneib J. P., 2009, A&A, 498, 37
Richard J. et al., 2010, MNRAS, 402, L44
Riley S., Bruursema J., Ford H. C., Zekser K. C., Infante L., Postman M., 2008, A&AS, 212, 1902
Riley S., Bruursema J., Ford H. C., Zekser K. C., Infante L., Postman M., 2009, BAAS, 41, 234
Rizza E., Morrison G. E., Owen F. N., Ledlow M. J., Burns J. O., Hill J., 2003, AJ, 126, 119
Sadeh S., Rephaeli Y., 2008, MNRAS, 388, 1759
Saha P., Read J. I., 2009, ApJ, 690, 154
Saha P., Williams L. L. R., 1997, MNRAS, 292, 148
Sharon K. et al., 2005, ApJ, 629, 73
Stark D. P., Ellis R. S., Richard J., Kneib J.-P., Smith G. P., Santos M. R., 2007, ApJ, 663, 10
Stott J. P., Smail I., Edge A. C., Ebeling H., Smith G. P., Kneib J.-P., Pimbblet K. A., 2007, ApJ, 661, 95
Struble M. F., Rood H. J., 1987, AJ, 93, 1035
Struble M. F., Rood H. J., 1999, ApJS, 125, 35
Umetsu K., Broadhurst T., 2008, ApJ, 684, 177
Umetsu K. et al., 2009, ApJ, 694, 1643
Umetsu K., Medezinski E., Broadhurst T., Zitrin A., Okabe N., Hsieh B. C., Molnar S. M., 2010, ApJ, 714, 1470
Valls-Gabaud D., Cabanac R., Lidman C., Diego J. M., Saha P., 2006, in Mamon G. A., Combes F., Deffayet C., Fort B., eds, EAS Publ. Ser. Vol. 20, Mass Profiles and Shapes of Cosmological Structures. EDP Sciences, Les Ulis, p. 149
Zheng W. et al., 2009, ApJ, 697, 1907
Zitrin A., Broadhurst T., 2009, ApJ, 703, L132
Zitrin A., Broadhurst T., Rephaeli Y., Sadeh S., 2009a, ApJ, 707, L102
Zitrin A. et al., 2009b, MNRAS, 396, 1985
Zitrin A., Broadhurst T., Barkana R., Rephaeli Y., Benítez N., 2010, preprint (arXiv:1002.0521)

This paper has been typeset from a TEX/LATEX file prepared by the author.